Optical spectroscopy of $(MnO_4)^{3-}$ and $(VO_4)^{5-}$ in $Sr_{10}(VO_4)_6F_2$

1997 J. Phys.: Condens. Matter 9 9893

(http://iopscience.iop.org/0953-8984/9/45/017)

J. Phys.: Condens. Matter **9** (1997) 9893–9908. Printed in the UK PII: S0953-8984(97)76589-5

Optical spectroscopy of $(MnO_4)^{3-}$ and $(VO_4)^{5-}$ in $Sr_{10}(VO_4)_6F_2$

M A Scott, B Henderson, H G Gallagher and T P J Han
Department of Physics and Applied Physics, University of Strathclyde, Glasgow G1 1XN, UK

Received 23 July 1996, in final form 11 July 1997

Abstract. The $3d^2$ configuration ions Mn^{5+} and V^{3+} have been incorporated in strontium fluorovanadate (SVAP) crystals grown using the Czochralski technique. Such crystals provide fourfold-coordinated sites for occupancy by the Mn^{5+} and V^{3+} ions, which are located near the centres of their respective tetrahedrally bonded molecular ions $(MnO_4)^{3-}$ and $(VO_4)^{5-}$. The optical absorption spectra of these ions are in the range 500 nm to 1100 nm and feature a number of overlapping bands related to the splittings of the ^1E, $^3T_2$ and $^3T_1$ excited states by the distorted tetrahedral crystal field. In terms of point-ion crystal field theory strong- and weak-field descriptions are appropriate to $(MnO_4)^{3-}$ and $(VO_4)^{5-}$ molecular ions respectively. This is confirmed for $(MnO_4)^{3-}$ by photoluminescence spectra which reveal sharp zero-phonon lines attended by vibronic structure characteristic of coupling to molecular vibrations of both $(MnO_4)^{3-}$ and the host $(VO_4)^{5-}$ ion. Luminescence from the $(VO_4)^{5-}$ ion is quenched by efficient nonradiative decay at all temperatures between 10 and 300 K.

The energy level structure of these $3d^2$ ions has been calculated using group theory assuming reductions in symmetry from T_d to C_{3v} to C_s. A comparison of the calculated level structure with the absorption and luminescence spectra shows that $(MnO_4)^{3-}$ and $(VO_4)^{5-}$ occupy distorted tetrahedral sites in SVAP. Selection rules derived for all transitions assuming C_s symmetry account for all the features in the absorption spectra of $(MnO_4)^{3-}$ and $(VO_4)^{5-}$ and in the photoluminescence spectrum of $(MnO_4)^{3-}$.

1. Introduction

The development of the Cr^{4+}:$MgSiO_4$ (forsterite) laser stimulated searches for other Cr^{4+}-based laser systems, not least because in forsterite the Cr ions occur in several different charge states and symmetry sites [1–3]. Similar effects occur in the $A_3B_2C_3O_{12}$ garnets, where Cr^{6+}, Cr^{4+} and Cr^{3+} ions are partitioned between tetrahedral C sites (Cr^{6+} and Cr^{4+}) and octahedral B sites (Cr^{3+}) in crystals co-doped with Cr and Ca^{2+} ions [4–6]. The authors have undertaken a survey of these $3d^2$ ions in laser hosts involving (i) the development of crystal growth and post-growth annealing techniques to optimize the Cr^{4+} ion concentration in crystals where multiple sites are available and (ii) searches for crystals where only a single tetrahedral site is available for occupancy by Cr^{4+} ions [7].

The crystal field splittings of multi-electron energy levels arise from the effects of even-parity terms (i.e. terms of order r^4, r^6, ...) in the crystal field Hamiltonian. For tetrahedral sites the r^4 term has the same functional form as in the octahedral case. Since the cation–anion separation in tetrahedral symmetry is $\sqrt{3}a$, where a is the length of the unit cube, the tetrahedral splitting of the e and t_2 single-electron levels is reduced by a factor $\frac{4}{9}$ and of opposite sign: the octahedral (Δ_O) and tetrahedral (Δ_T) crystal field splittings are related by

$$\Delta_O = 10\ \mathrm{Dq} = -(\tfrac{9}{4})\Delta_T \tag{1}$$

0953-8984/97/459893+16$19.50

where $\mathrm{Dq} = (Ze^2/4\pi\varepsilon_0)(\langle r^4\rangle_{3d}/6a^5)$ [8, 9]. The magnitude of Dq may be manipulated by varying the anion–cation separation, the charge $-Ze$ on the ligand anion and the effective positive charge on the central cation.

The splittings and ultimate ordering of the free ion levels in crystals are determined by the interplay between the crystal field interaction and electron–electron interactions on the central and neighbouring ions. This interplay may be represented on a Tanabe–Sugano plot of the energy level $E(\Gamma_i)/B$ as a function of crystal field strength Dq/B for constant C/B. Equation (1) implies that the energy level structure of $3d^n$ ions in tetrahedral sites is equivalent to that of $3d^{10-n}$ ions in octahedral fields and may be represented by the same Tanabe–Sugano diagram [8, 9]. The Tanabe–Sugano plot for $3d^2$ ions in figure 1 shows that the low-lying excited levels $^1\mathrm{E}$ and $^3\mathrm{T}_2$ are degenerate near $\mathrm{Dq}/B \simeq 1.4$. This level crossing roughly divides the energy level diagram into weak crystal field ($\mathrm{Dq}/B < 1.4$) and strong crystal field ($\mathrm{Dq}/B > 1.4$). The Cr^{4+}-doped garnets $Y_3Al_5O_{12}$ (YAG) and $Y_3Ga_5O_{12}$ (YGG) for which $\mathrm{Dq}/B \simeq 1.44$ appear to be strong-field systems, in which case the luminescence should be characterized by sharp zero-phonon lines and weak vibronic structure. The observed luminescence spectra are broadband $^3\mathrm{T}_2 \rightarrow {}^3\mathrm{A}_2$, showing that the weak-crystal-field description is the more appropriate. Apparently, categorization as to strong or weak must take into account lattice relaxation after excitation [10].

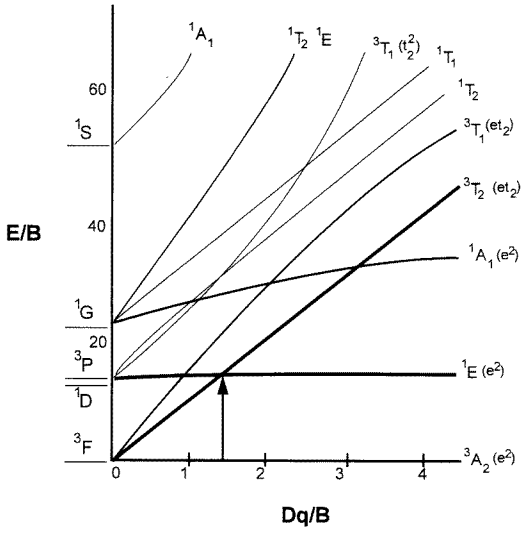

Figure 1. Tanabe–Sugano energy level diagram for $3d^2$ ions in a tetrahedral field. The energies have been calculated for the $3d^8$ system in octahedral fields assuming $C/B = 4.4$. The free ion levels in the absence of a crystal field, i.e. $\mathrm{Dq} = 0$, are shown on the left. The levels marked in bold are those identified in the absorption/luminescence spectra.

This paper is concerned with the optical properties of Mn^{5+} and V^{3+} ions in strontium fluorovanadate, $Sr_{10}(VO_4)_6F_2$ (SVAP), a crystal particularly suited for isomorphic substitution of Mn^{5+} ions at the pentavalent, fourfold-coordinated $(VO_4)^{3-}$ site. Earlier studies showed that Mn^{5+} was stable in tetrahedral sites in calcium chloroapatite, $Ca_{10}(PO_4)_6Cl$ and spodiosite, Ca_2PO_4Cl [11]. Recently, Oetliker *et al* [12] have reviewed the doping of Mn^{5+} ions in the calcium and strontium choro-apatites, chloro-spodiosites and the Li_3PO_4-type salts, in which Mn^{5+} luminescence is characterized by sharp zero-phonon lines and weak phonon replicas. Three-level laser action at room temperature has

been reported for Mn^{5+} in $Ba_3(VO_4)_2$ ([13], Merkle *et al* 1992) a crystal which like SVAP has pentavalent tetrahedral sites for Mn substitution, thereby minimizing the likelihood of multiple Mn valence states [14].

2. Energy levels and transitions

The energy level splittings and selection rules required to interpret the polarized absorption and photoluminescence spectra of $3d^2$ ions in distorted tetrahedral sites are determined by group theory [8, 9]. An x-ray determination of the V^{5+}–O^{2-} bond lengths in SVAP, table 1, shows that the $(VO_4)^{3-}$ coordination tetrahedron is stretched along the *c* axis such that the O(2) ion is further away from the V^{5+} ion than the other three O^{2-} ions [15]. In view of this even-parity distortion along the *c* axis the symmetry of the $(VO_4)^{3-}$ tetrahedron is reduced from T_d to C_{3v} ([13], Merkle *et al* 1995). Other angular distortions of the tetrahedron reduce the symmetry from C_{3v} to C_s [16].

Table 1. Bond lengths of the $(VO)_4$ tetrahedron in SVAP [15].

	Bond Length (nm)
V–O(1)	0.1716
V–O(2)	0.1721
V–O(3)	0.1703
V–O(4)	0.1703

The splitting patterns of the energy levels of the $3d^2$ ion are deduced by comparing the elements of the character tables of T_d, C_{3v} and C_s. For example, the $^3T_2$ irreducible representation of the T_d group decomposes into $^3A_1$ and ^3E representations in C_{3v} symmetry, each irreducible representation having a different energy. The character table for C_{3v} symmetry confirms that only orbital singlets (A_1, A_2) and orbital doublet (E) levels are permitted in C_{3v} symmetry. Further reduction in symmetry from C_{3v} to C_s shows that A_1 and A_2 levels now transform as the irreducible representations A' and A'' and orbital doublets E split into orbital singlets A' and A''. The orbital splittings of the low-lying energy levels of $3d^2$ ions in T_d, C_{3v} and C_s symmetries are summarized in figure 2, assuming strong crystal fields such that ^1E is the lowest-lying level in T_d symmetry.

The probabilities of transitions between states Γ_1 and Γ_2 are proportional to the matrix element $\langle\Gamma_1|\boldsymbol{\mu}|\Gamma_2\rangle$, where $\boldsymbol{\mu}$ is a dipole operator. Consequently, the selection rules for the $\Gamma_1 \rightarrow \Gamma_2$ transition are determined by comparing the function spaces in the character tables which transform as the direct product $\Gamma_1 \times \Gamma_2$. The π- and σ-polarized electric dipole (ED) operators transform as z and x, y respectively, while π- and σ-polarized magnetic dipole (MD) operators transform as R_x, R_y and R_z [9]. By inspection of the character tables for the T_d group it is evident that the ED operator transforms as T_2. Since $A_2 \times T_1 = T_2$ the $^3A_2 \rightarrow {}^3T_1$ transition of the $3d^2$ ion in tetrahedral sites is an allowed ED transition in both π and σ polarization. All other ED transitions are forbidden. Extension of this analysis to the cases of C_{3v} and C_s symmetry are straightforward and yield the selection rules given in table 2 and illustrated in figure 2.

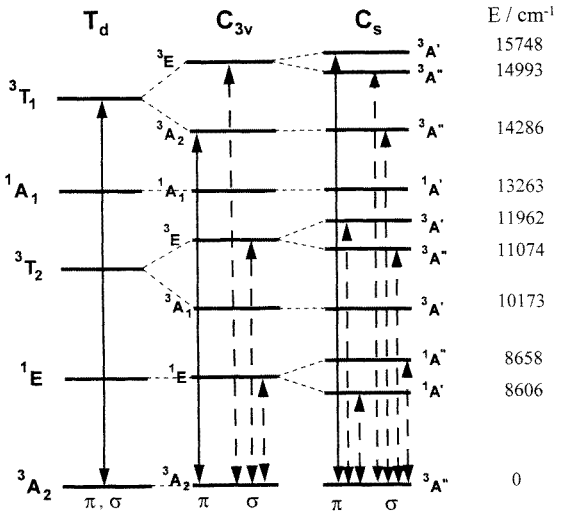

Figure 2. Schematic representation of the energy level structure of Mn^{5+}:SVAP according to the reduction of symmetry $T_d \rightarrow C_{3v} \rightarrow C_s$. The predicted electric dipole polarizations are shown and the assignments of the energies determined from the absorption spectrum given. The full arrows denote allowed transitions while dashed arrows indicate partially allowed transitions. On the right-hand side the energy level assignments are based on the absorption spectra of Mn^{5+}.

Table 2. Polarization selection rule table for C_{3v} and C_s symmetry.

		Initial state		
C_{3v}	Final state	A_1	A_2	E
	A_1	ED(π)	MD(π)	ED(σ) MD(σ)
	A_2	MD(σ)	ED(π)	ED(σ) MD(σ)
	E	ED(σ) MD(σ)	ED(σ) MD(σ)	ED(π), ED(σ) MD(π), MD(σ)
C_s		A'	A''	
	A'	ED(σ) MD(π)	ED(π) MD(σ)	
	A''	ED(π) MD(σ)	ED(σ) MD(π)	

Note: In this notation π polarization implies that the E vector of the radiation oscillates parallel to the symmetry axis. For σ polarization the E vector is perpendicular to the symmetry axis. The symmetry axis may be internal to the crystal or an externally applied field.

3. Experimental techniques

Mn^{5+}-doped SVAP crystals were grown by the Czochralski technique at high temperatures (1923 ± 20 K) in an Ir crucible. Because V_2O_5 is somewhat unstable at high temperatures it is reacted with $SrCO_3$ at 1573 K to form strontium orthovanadate, $Sr_9(VO_4)_6$, which is then melted with 1–5 mol% excess of SrF_2 to compensate for evaporation losses at high

temperature. Using seed crystals nucleated on an Ir wire, high-quality SVAP crystals were grown with typical dimensions 15–18 mm diameter and 40–60 mm in length, using a growth rate of 30 μm s^{-1} and a rotation rate of $\pi/2$ rad s^{-1}.

Optical absorption measurements were made using samples of size $5 \times 2 \times 2$ mm^3. The absorption coefficient was recorded with an AVIV-Cary 14 dual-beam spectrophotometer at 300 K and 77 K. At this latter temperature the sample was held on a cold finger in the vacuum chamber of a liquid nitrogen cryostat. The wavelength range covered by the spectrophotometer was 170–2000 nm. Luminescence was excited using the all-line output from a 4.5 W argon ion laser, or rhodamine 6G or Ti-sapphire lasers pumped by the 4.5 W argon ion laser. Both the dye laser and Ti-sapphire laser used birefringent tuning elements in astigmatically compensated cavities to effect narrow-bandwidth selectivity of the tunable laser outputs, 570–625 nm (R6G dye) and 700–820 nm (Ti-sapphire). The laser beam was focused onto the sample fixed to the cold-finger He refrigerator fitted with four mutually orthogonal quartz windows for sample access by the absorbed and egress by the emitted beams. The pump beam was chopped mechanically to provide a square wave reference beam for improved signal/noise ratio using phase sensitive detection. Emitted radiation is focused onto the entry slit of a 0.5 m grating monochromator. After dispersal by the monochromator the luminescence is converted to an electrical signal by a cooled Ge photodetector or GaAs photomultiplier tube. This electrical signal is compared with the reference signal by a dual-phase lock-in amplifier and processed by a differential amplifier and microcomputer.

In photoluminescence decay time measurements the samples were excited by an N_2 laser pumped dye laser. The emitted light is dispersed in a 0.2 m monochromator and detected by a cooled Ge photodetector, pre-amplified and stored in a digital oscilloscope. The sample is mounted on the cold finger of a closed-cycle He refrigerator which permitted measurements as short as 1 μs.

4. Results and discussion

4.1. Annealing treatments

Crystals of undoped SVAP were grown in a pure N_2 atmosphere: they were light to dark green in colour, the gradation being from top to bottom of the boule. A typical optical absorption spectrum is shown in figure 3(a). Since $3d^2$ configuration ions have large stabilization energies in T_d symmetry this near-infrared absorption is assigned to V^{3+} ions present because of evaporation from the melt of both oxide and fluoride species during growth. Although present in rather small concentrations, the large absorption coefficient for the V^{3+} species is in accord with their presence at tetrahedral sites: a large absorption cross section for d–d transitions is evident because their transition probability is strongly enhanced by the odd-parity component of the crystal field. The assignments given for the bands at ~500 nm ($^3A_2 \rightarrow {}^3T_1$ (t_2^2)), at 675–920 nm ($^3A_2 \rightarrow {}^3T_1$ (et_2)) and ~1000 nm ($^3A_2 \rightarrow {}^3T_2$) are based on their similarity with the spectra of Cr^{4+} and Mn^{5+} ions in other hosts [14, 16, 18]. Since such bands would compete with Mn^{5+} and Cr^{4+} luminescence they must be eliminated. This is achieved by $V^{3+} \rightarrow V^{5+}$ oxidation in post-growth annealing at 1573 K in air for 10–12 hours. Slow heating and cooling rates of 0.5 K min^{-1} were used to avoid cracking. After such oxidation treatments the SVAP crystals show little significant optical absorption between 550 nm and 1.5 μm (figure 3(b)).

Optical absorption spectra of as-grown Mn-SVAP crystals have identical spectral features to those in figure 3(b): the absence of absorption bands from Mn^{5+} ions in tetrahedral sites confirm that any Mn is present in a valence state and symmetry site in which it does

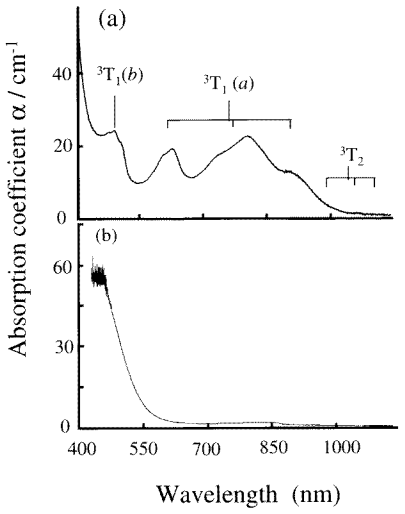

Figure 3. Showing the unpolarized optical absorption spectra at 300 K of (a) undoped SVAP in the wavelength range 350–1350 nm and (b) undoped SVAP after oxidizing anneal at 1273 K.

not absorb visible or near-infrared radiation. After annealing the as-grown crystals in air at 1273 K for 12 hours the SVAP crystals are deep blue in colour, as are Cr^{4+}-doped crystals of $MgSiO_4$, $Ca_5(PO_4)_3F$ (CFAP) and $SrGdGa_3O_7$ (SGGM). This result suggests that growth under equilibrium conditions results in Mn being formed in a lower valence state even though a pentavalent site is available for substitution by the Mn^{5+} ion [14]. A spectrum such as that in figure 3(b) shows that the as-grown crystal absorbs strongly in the near-UV and blue spectral regions but only weakly at $\lambda = 700$ nm indicating that only trace amounts of Mn^{5+} are present. The absorption transitions of Mn^{2+} normally occur in the UV region between 150 and 250 nm. The observed spectrum implies that in the crystals grown under nitrogen atmospheres the Mn^{2+} ions occupy the Sr^{2+} site. High-temperature annealing under oxidizing conditions converts Mn^{2+} to Mn^{5+}, these ions being stabilized in the tetrahedral sites. Tetrahedrally coordinated Mn^{5+} does not exist in the as-grown crystal since none of the expected visible and near-infrared absorption bands are observed.

4.2. Crystal field spectra

The similarities between the spectra of undoped SVAP as grown and thermally treated, with those of the as-grown Mn-doped SVAP are clear. Neither show spectra in the wavelength range 550 nm to 1.5 μm, confirming the absence of V^{3+} (figure 3(b)) or Mn^{5+}. The polarized absorption spectra of Mn^{5+}:SVAP shown in figure 4 were measured at 300 K after annealing in air. The spectrum is dominated by the strong electric-dipole-allowed transitions from the $^3A_2$ (e^2) ground level to the $^3T_1$ (et^2) level. The $^3A_2$ and $^3T_1$ states derive from different strong-field orbitals which are characterized by different strengths of electron–lattice coupling. As a consequence, the observed absorption is broadband at all temperatures. The width of the band is $\sim$200 nm at room temperature and the spectral features are in general agreement with those reported by Merkle *et al* ([13], 1995). As figures 3(a) and 4 show the $^3A_2 \rightarrow {}^2T_1$ band is composed of three overlapping components: for $3d^2$ ions in pure T_d site symmetry there should be a single band. These overlapping

bands are due to splitting of the $^3T_2$ level (tetrahedral) by the lower-symmetry distortions appropriate to C_s symmetry at the (VO_4) molecular ion. The π- and σ-polarized absorption spectra in figure 4 confirms that the two π-polarized $^3A'' \rightarrow {}^3A''$, $^3A''$ transitions occur at lower photon energies than the $^3A'' \rightarrow {}^3A'$ transition in agreement with the energy level structure given in figure 2. As indicated in table 2 the $^3A'' \rightarrow {}^3A''$, $^3A''$, $^3A'$ are all allowed electric dipole transitions since they are derived from the allowed $^3A_2 \rightarrow {}^3T_1$ transition in tetrahedral symmetry.

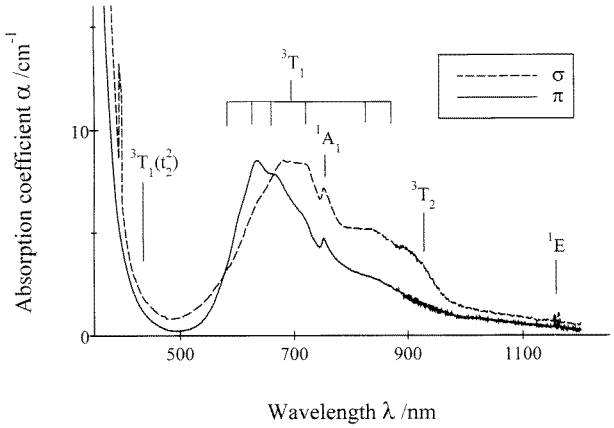

Figure 4. Polarized optical absorption spectra recorded at 77 K for Mn^{5+}-doped SVAP. The assignments refer to the T_d model of the site symmetry.

A further weak band in figure 4 near 850–950 nm is attributed to the electric-dipole-'forbidden' $^3A_2 \rightarrow {}^3T_2$ transition in T_d symmetry, which is also split into three components. The splittings and polarization patterns of these transitions also are associated with the symmetry reductions from T_d to C_s. A very weak absorption near 460 nm is assigned to the spin-allowed $^3A_2$ $(e^2) \rightarrow {}^3T_1$ (t_2^2) transition. This latter transition requires a two-electron 'jump' in the change of electron configuration, so violating the configuration selection rule [8]. There are some relatively sharp features near ~750 nm and 1160 nm, which correspond to the $^3A''(^3A_2) \rightarrow {}^1A'(^1A_1)$ and $^3A''(^3A_1) \rightarrow {}^1A'(^1E)$, $^1A''(^1E)$ absorption transitions, respectively. Since these levels are derived from the same (e) strong-field configuration they are characterized by similar Huang–Rhys factors, so that sharp zero-phonon line transitions result. The room-temperature widths of these lines are only ~12 cm^{-1}. The resolved doublet at 1162 nm and 1155 nm has been reported in other hosts, implying that the orbital degeneracy of the ^1E level is removed by the low-symmetry crystal field. The orbital splitting of 53 cm^{-1} in the ^1E level measured at 300 K results from this distortion of the local T_d symmetry and is much smaller than the splittings measured for Mn^{5+} in chloroapatites and spodiosites [12]. All these transitions are forbidden in pure tetrahedral symmetry. They become partially allowed transitions in C_s symmetry because odd-parity crystal field distortions admix opposite-parity ligand orbitals into the central transition metal ion orbitals [10].

Comparing the optical absorption coefficients at 650 nm for slices from the top and bottom of the boules allows the effective segregation coefficient of Mn^{5+} in SVAP, $k_{eff} = 0.03$, to be measured [14]. Since in the initial melt the concentration of Mn^{4+} was 1×10^{20} ions cm^{-3} the estimated Mn^{5+} concentration in the crystal is $\sim 2.6 \pm 0.5 \times 10^{18}$ ions cm^{-3}. From the peak absorption coefficient of 16 cm^{-1} the absorption cross

section of $\sigma_{abs} \sim 6.0 \pm 1.2 \times 10^{-18}$ cm^2 is calculated for the $^3A_2 \rightarrow {}^3T_1$ transition at 650 nm. A typical value for the $^4A_2 \rightarrow {}^4T_2$ transition of Cr^{3+} ions in distorted octahedral sites is $\sigma \sim 10^{-20}$ cm^2. The larger value in Mn^{5+}:SVAP follows from the static odd-parity crystal field terms at tetrahedral crystal field sites, which admix the 3d states of the Mn^{5+} with the s and p ligand field orbitals and introduce opposite-parity character into the 3d wavefunctions [10]. Alternatively, admixture can occur with lower-lying and fully occupied, odd-parity states of the central ion with the 3d states [11]. Consequently, the Laporte selection rule is relaxed and transitions can occur by the electric dipole mechanism.

The crystal field parameters derived from the point-ion theory [8, 9] are obtained by fitting the experimental data assuming T_d symmetry. Setting the ground state, $^3A_2$, as the zero of energy, the separation in energy from the lowest orbital triplet, i.e., $^3T_2$ (et_2), gives the quantity 10 Dq, where Dq measures the strength of the *tetrahedral* crystal field. The Racah parameters B and C are estimated from the positions of the $^3T_1$ and ^1E levels, respectively. For Mn^{5+} in SVAP, Dq is 1088 cm^{-1}. An assumed value of $Dq/B = 2.2$ places the $^3A_2 \rightarrow {}^3T_1(et_2)$ transition at $\lambda \sim 630$ nm, as given by the absorption spectrum in figure 4. (The energies of the $^3T_2$ and $^3T_1$ levels are determined from the centres of gravity of the crystal field split $^3A_2 \rightarrow {}^3T_2$, $^3T_1$ transitions.) The energy of the ^1E level is almost independent of the crystal field strength, being given by $E(^1E) = 8B + 2C$ [18]. Using the average position of the doublet absorption peaks of 8600 cm^{-1} and $B = 518$ cm^{-1} gives $C = 2321$ cm^{-1}. The ratio $C/B = 4.4$ agrees well with the free-ion value of 4.2 for the Cr^{4+} ion [17, 18]. This crystal field interpretation of the observed spectra shows that Mn^{5+} in SVAP behaves as a relatively high-field ion ($Dq/B \sim 2.2$), despite the intrinsically weak crystal field at tetrahedral sites. Since the estimated value of Dq/B is higher than the cross-over point of the ^1E and $^3T_2$ levels, the luminescence spectrum should be dominated by the $^1E \rightarrow {}^3A_2$ transition.

The Slater parameters are related to the Racah parameters by the simple relations

$$F^{(2)} = 7(7B + C) \tag{2}$$

$$F^{(4)} = \frac{63}{5}C \tag{3}$$

which yields values of $F^{(2)} = 41\,629$ cm^{-1} and $F^{(4)} = 29\,245$ cm^{-1}, both substantially reduced from the free-ion values of $F^{(2)} = 91\,427$ cm^{-1} and $F^{(4)} = 56\,625$ cm^{-1} [18]. The reduced Slater parameters result from the delocalization of the transition metal ion wavefunction and are referred to as the *nephelauxetic effect*. As cation charge increases from V^{3+}, Cr^{4+} to Mn^{5+} there is a strong tendency to form covalent bonds with neighbouring ligand ions. The calculated reductions of the Slater parameters, $\Delta F^{(k)}$, from the Mn^{5+} free-ion values, can be explained using molecular orbital theory. The overlap of the t_1 and t_2 oxygen orbitals with the Mn^{5+} 3d (e) wavefunctions partially shields the effective Mn core charge. Furthermore, the e orbital of the $(MnO_4)^{3-}$ molecular ion is expanded relative to the Mn^{5+} free ion by *covalent* bonding and the e orbitals then contain an admixture of ligand orbitals. The effect of covalency is pronounced by the large size and polarizability of the O^{2-} ions and the high-charge state of the Mn^{5+} ion.

4.3. Mn^{5+} photoluminescence and decay times

Although there is strong $^1E \rightarrow {}^3A_2$ luminescence from $(MnO_4)^{3-}$ in SVAP there is no luminescence signal from the trace amounts of $(VO_4)^{5-}$ present in as-grown, undoped SVAP. In this weak-crystal-field system the excited $(VO_4)^{5-}$ ions decay nonradiatively. The fluorescence spectrum of $(MnO_4)^{3-}$:SVAP measured at 300 K and 14 K and excited with

the chopped output of a Ti-sapphire laser at $\lambda = 800$ nm is shown in figure 5(a). Excitation therefore occurs into the $^3T_2(^3A')$ band and nonradiative relaxation then proceeds across an energy gap of $\sim$3400 cm^{-1} to the lowest excited state (^1E). For the fluorescence spectrum at 300 K there are five peaks in the wavelength range $\lambda = 1$–1.35 μm including a very strong double peak at 1155 and 1162 nm assigned to the zero-phonon lines of the $^1E(^1A'')$ and $^1E(^1A') \rightarrow {}^3A_2$ transitions respectively, as a consequence of C_s symmetry reduction. This confirms the earlier strong-crystal-field prediction for Mn^{5+}:SVAP (section 4.2). The peaks at 1.21 μm and 1.27 μm decrease monotonically in intensity with increasing wavelength, being typical of the Stokes-shifted vibronic sidebands of the zero-phonon line. Such weak sidebands result from the coupling of the electronic states to the vibrational modes of the $(MnO_4)^{3-}$ molecular ion [9, 20]. At room temperature there is also a very weak band at 1125 nm, the thermally activated anti-Stokes sideband of the zero-phonon line. The integrated intensity of the zero-phonon line, I_{zpl}, relative to the full band, I_0 including the vibronic sideband is given by

$$\frac{I_{zpl}}{I_0} = \exp(-S). \tag{4}$$

Experimentally, the measured ratio $I_{zpl}/I_0 = 0.88$ corresponding to a Huang–Rhys factor of $S \simeq 0.13$. The doublet structure apparent in the 1164 nm line is more clearly defined at lower temperatures by virtue of the large reduction in linewidth, from $\sim$85 cm^{-1} at 300 K to $\sim$6 cm^{-1} at 10 K. The zero-phonon line shifts to longer wavelengths with increasing temperature, this red shift being of order 17 cm^{-1} at 300 K due primarily to the effects of lattice expansion.

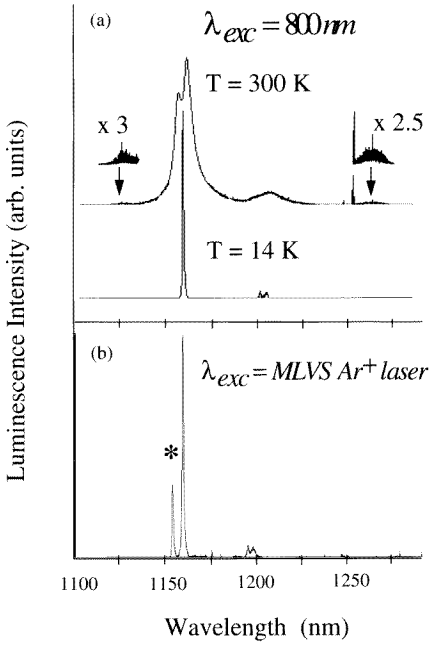

Figure 5. Luminescence spectra of Mn^{5+}:SVAP. In (a) the luminescence was excited using a Ti:Al_2O_3 laser with output at $\lambda = 800$ nm and detected at both 14 K and 300 K. The spectrum in (b) was recorded at $T = 14$ K after excitation by the resonance lines of an Ar^+ laser.

Excitation by the multiple resonance lines of an Ar^+ laser at $T = 14$ K reveals the presence of an additional strong transition at 1154 nm on the high-energy side of the zero-phonon line, as shown in figure 5(b). This transition has one-third of the intensity of the main zero-phonon line at low temperature. As the temperature is raised this additional peak quickly disappears. This different temperature dependence from the main zero-phonon line implies that the additional peak originates from a different type of Mn centre than that which contributes to the main luminescence. As figure 5(a) shows, when selectively excited by a narrow-band Ti^{3+}:Al_2O_3 laser at $\lambda = 800$ nm, this additional peak disappears since only the subset of absorption lines corresponding to the main site are excited.

The luminescence decays of the $^1E \rightarrow {}^3A_2$ zero-phonon lines excited using the pulsed output from the DCM dye laser operating at 670 nm are singly exponential corresponding to lifetimes of 395 μs and 585 μs at $T = 300$ K and $T = 30$ K, respectively, in excellent accord with lifetimes of the $^1E \rightarrow {}^3A_2$ transition in chloride hosts [16, 18, 19] but are substantially shorter than those reported by Merkle *et al* ([13], 1995) (475 μs and 980 μs respectively). This discrepancy could be explained by the differences in the concentration of the Mn dopant in the samples used by the two groups: the concentration of the Mn ions mentioned above corresponds to 0.11 at.% as compared to 0.06 to 0.07 at.% reported by Merkel and his co-workers. This suggest the possibility of concentration quenching in this crystal host. The small decrease in lifetime at higher temperatures is attributed to weak non-radiative relaxation. In Mn^{5+}:SVAP, the relatively short lifetime indicates that the $^1E \rightarrow {}^3A_2$ luminescence occurs by an electric dipole process, the transition probability being greatly enhanced by static and dynamic odd-parity distortions at the covalently bonded tetrahedral site. The energy separation between the 3d states and the odd-parity ligand field states is reduced by molecular bonding, thereby increasing the extent of wavefunction admixture and hence the strength of the induced electric dipole moment [9].

4.4. Polarized optical transitions of $(MnO_4)^{3-}$ in SVAP

The overlapping absorption spectra and their polarizations require a more complex splitting of levels for the $(VO_4)^{5-}$ and $(MnO_4)^{3-}$ molecular ions than is obtained assuming T_d symmetry. The x-ray data are consistent with a distortion of the MO_4 tetrahedron from T_d to C_{3v} symmetry. Polarized absorption and luminescence spectra in figures 4–6 confirm that other distortions are present which reduce the symmetry from C_{3v} to C_s. These distortions remove any remaining orbital degeneracy so that the doubly degenerate E levels are split into singly degenerate A′ and A″ levels. The group theoretical analysis of the selection rules for $3d^2$ ions in C_s sites summarized in figure 2 and table 2 accounts for all the optical absorption and luminescence spectra in figures 3–6. The energy values quoted on the right-hand side of figure 2 have been calculated using the centres of gravity of the polarization spectra showed and assuming C_{3v} symmetry. Which of the A′ and A″ components of a particular E level is highest has been determined from the senses of polarization shown in figures 4–6.

Since Mn^{5+}:SVAP is a strong-crystal-field system, the main effect of the spin–orbit interaction is to mix states from different configurations differing in ΔS by ± 1. The degree of mixing, Δ, depends on the spin–orbit coupling constant, ζ, and the difference in energy between spin singlet ($S = 0$) and triplet ($S = 1$) states and is given by

$$\Delta = \frac{\langle \Psi_T | H_{SO} | \Psi_S \rangle}{E_T - E_S} \tag{5}$$

where $E_T - E_S$ is the energy difference between the states and the spin–orbit coupling energy, H_{SO}, depends on the magnitude of the constant ζ [9]. Essentially, the singlet

transition 'borrows' intensity from the nearest, higher-lying triplet transition, their relative intensities being

$$\frac{I_S}{I_T} = \left(\frac{\zeta}{E_T - E_S}\right)^2. \tag{6}$$

The free-ion value of $\zeta \simeq 460$ cm^{-1} for Mn^{5+} is reduced in crystals by the nephelauxetic effect to ~120 cm^{-1}. The energy difference in figure 4 between ^{1}E and ^{3}E (^{3}T$_2$) is $E_T - E_S \sim 2900$ cm^{-1}. The corresponding separation in energy for the ^{1}A$_1$–^{3}A$_2$(^{3}T$_1$) states is ~1000 cm^{-1}. Because of the triplet state mixing into singlet states the $\Delta S = 0$ selection rule is somewhat relaxed. In consequence, triplet → singlet absorption transitions ^{3}A″ (^{3}A$_2$) → ^{1}A′ (^{1}A$_1$) and ^{3}A″ (^{3}A$_2$) → ^{1}A′, ^{1}A″ (^{1}E) occur quite strongly by electric dipole processes. The greater intensity of the ^{3}A″ (^{3}A$_2$) → ^{1}A′ (^{1}A$_1$) relative to the ^{3}A″ (^{3}A$_2$) → ^{1}A′, ^{1}A″ (^{1}E) transitions reflects the greater triplet mixing predicted by equations (5) and (6). The observed intensities of the ^{3}A″ (^{3}A$_2$) → ^{1}A′ (^{1}A$_1$), and ^{1}A′, ^{1}A′ (^{1}E) transitions are similar to those of the chloroapatites and spodiosites as reported by Oetliker *et al* [12]. A simplified crystal-field model of Mn^{5+} in $Sr_5(PO_4)_3Cl$ estimated that the ^{1}E and ^{1}A$_1$ states contained ~40% triplet character, respectively [17].

The polarization of the ^{1}A′, ^{1}A″ → ^{3}A″ luminescence is shown in figure 6. The doublet structure of the zero-phonon line is caused by the splitting of the ^{1}E level in C$_s$ symmetry sites. These spectra were excited by the π-polarized output of the Ti-sapphire laser tuned to 800 nm, which selectively excites the ^{3}A″ (^{3}A$_2$) → ^{3}A″ (^{3}T$_2$) transition of Mn^{5+}. The luminescence intensity follows a $\cos^2(\theta_e)$ dependence on the polar angle θ_e with maximum intensity for the π polarization ($\theta_e = 0°$). For the 1164 nm line $I_\pi/I_\sigma = 2.6$ and for the peak at 1159 nm $I_\pi/I_\sigma = 1.9$ which ratios according to figure 2 and table 3 agree with the pure π- and σ-polarization characteristics of ^{1}A″ (^{1}E) → ^{3}A″ (^{3}A$_2$) and ^{1}A′ (^{1}E) → ^{3}A″ (^{3}A$_2$), respectively.

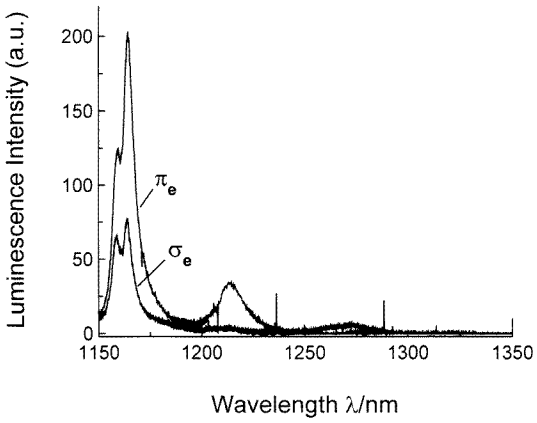

Figure 6. Polarized luminescence spectra of Mn^{5+}:SVAP at 14 K excited using the Ti:Al_2O_3 laser at 800 nm. (The π_e- and σ_e-polarization labels refer to $\boldsymbol{E} \parallel c$ axis and to $\boldsymbol{E} \parallel a$ axis of the emitted radiation.)

The ^{1}A″ → ^{3}A″ luminescence at room temperature is due to thermal population of the ^{1}A″ level. Assuming a splitting of 53 cm^{-1} between the absorption lines, implies that the ^{1}A″ component contains ~44% of the ^{1}E population at 300 K for levels in thermal equilibrium. At 10 K, this population ratio is only 0.05% and the luminescence is almost

Table 3. Summary of the absorption transitions of the $(MnO_4)^{3-}$ ion in SVAP assigned, assuming T_d site symmetry.

Transition from ground state $^3A_2$ ($t_1^6e^2$) to excited state	Observed energies (cm^{-1}) MnO_4^{3-}	VO_4^{5-}
^1E	8605	—
	8658	—
$^3T_2$	10 100	9302
$^1A_1$	13 262	—
$^3T_1$	14 577	12 422
$^3T_1$	16 130	15 625
$^1T_2$	—	—
$^3T_1$	23 800	20 408

entirely from the $^1A'$ level as observed in figure 5(a). There is no photoluminescence signal from $^3A'$ ($^3T_2$) and $^3A''$ ($^3T_2$) which would appear as broad bands superimposed on the $^1E \rightarrow {}^3A_2$ zero-phonon lines. According to figure 2 the low-energy $^3A'$ ($^3T_2$) level is only $\sim$1600 cm^{-1} ($\Delta E \sim 8$ kT) above the ^1E state. Consequently, assuming that the energy levels are in thermal equilibrium, only $\sim$0.05% of the total excited population is in the $^3A''$ at 300 K and no broadband luminescence is expected at any temperature in the range 10 K–300 K.

4.5. Vibronic structure

The electronic states of an impurity ion couple either to the vibrational modes of the crystal or to local modes of the molecular ion. Figure 7 shows the vibronic structure associated with the $^1A' \rightarrow {}^3A''$ zero-phonon line at 8608 cm^{-1}: this plethora of sharp lines is typical of the local vibrational modes of a molecular ion [9, 21]. There are four fundamental vibrational modes of an undistorted XY_4 molecular ion, which transform as the a_1, e and $^2t_2$ irreducible representations of the T_d group, where a_1 is the totally symmetric stretching mode, e is a bending deformation and the two t_2 vibrations are stretching t_2 modes. The vibronic sidebands are weaker than the zero-phonon line and displaced from it by energy differences of up to 1200 cm^{-1}. The rather weak lines at displacements of 69 cm^{-1}, 102 cm^{-1} and 119 cm^{-1} are caused by coupling to the long-wavelength phonons of the crystal. Table 4 shows that neither the free $(VO_4)^{5-}$ nor $(MnO_4)^{3-}$ molecular ions have fundamental modes with energies below 300 cm^{-1}. The strongest modes are assigned to one- and two-quantum excitations of the fundamental modes of $(MnO_4)^{3-}$ and $(VO_4)^{5-}$, weaker peaks being combinations of fundamental and harmonic molecular vibrational modes with lattice modes. The detailed assignments in figure 7 reveal the near coincidence of mode energies for the $(MnO_4)^{3-}$ and $(VO_4)^{5-}$ molecular ions as a consequence of their similarity in molecular weights. In such instances resonances between the modes may account for many of the weak features evident in figure 7. The energies of the local modes coupled to the $^1E \rightarrow {}^3A_2$ transitions are changed by only $\sim$15 cm^{-1} relative to the free-ion values in table 4.

The vibronic progression of the local bending mode v_2 (e) of the $(MnO_4)^{3-}$ ion with energy 324 cm^{-1} is evidence of a dynamic Jahn–Teller effect in the excited state [16, 20]. The ^1E excited state or the $(MnO_4)^{3-}$ molecular ion in SVAP undergoes a dynamic Jahn–Teller distortion through coupling of local molecular vibrations of e symmetry to the orbitally

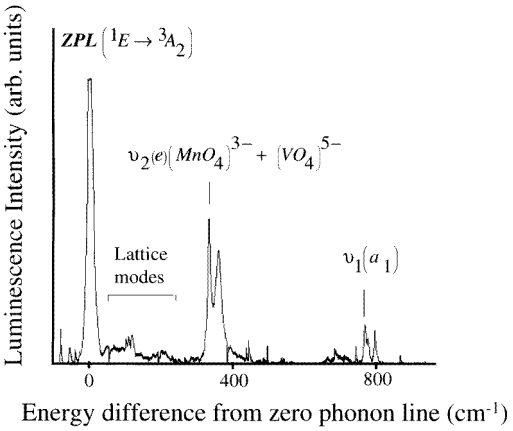

Figure 7. Vibronic spectrum of Mn^{5+}:SVAP with peaks measured relative to the zero-phonon line at 8608 cm^{-1}.

Table 4. Analysis of the vibronic structure in the NIR spectrum of Mn^{5+}-doped SVAP, where ΔE is the energy difference from the zero-phonon line at 8608 cm^{-1}.

Mode of vibration	Ionic species	Free-ion energies	SVAP energies	ΔE (cm^{-1}) theory
Lattice mode v_{L1}	—	—	69	—
Lattice mode v_{L2}	—	—	102	—
Lattice mode v_{L3}	—	—	119	—
v_2 (e)	$(MnO_4)^{3-}$	324	332	—
v_2 (e)	$(VO_4)^{3-}$	341	358	—
v_2 (e) + v_{L1}	$(MnO_4)^{3-}$	—	397	401
v_2 (e) + v_{L2}	$(MnO_4)^{3-}$	—	449	434
$2v_2$ (e)	$(MnO_4)^{3-}$	648	662	664
v_2 (e) + v_2(e)	$(VO_4)^{3-}$ $(MnO_4)^{3-}$	—	687	690
$2v_2$ (e)	$(VO_4)^{3-}$	682	715	716
$2v_2$ (e) + v_{L1}	$(MnO_4)^{3-}$	—	742	733
v_3 (t_2)	$(VO_4)^{3-}$	780	776	—
v_1 (a_1)	$(MnO_4)^{3-}$	838	795	—
v_1 (a_1) + v_{L1}	$(MnO_4)^{3-}$	—	867	862
$3v_2$ (e)	$(MnO_4)^{3-}$	972	1003	996

degenerate ^{1}E electronic state. That the v_2 (e) vibronic transitions are of greater intensity than the v_1 (a_1) transition shows that the coupling to Jahn–Teller modes in the excited state is stronger than coupling to symmetric modes. There are similar effects in the luminescence spectra of Mn^{5+}-doped vanadate crystals [16, 18] and in the F^+ centre in CaO [9]. In the optical absorption spectrum of the isomorphic host Mn^{5+}:$Sr_5(PO_4)_3Cl$ at $T = 2$ K the vibrational peaks are superimposed on a doublet electronic transition which was attributed to dynamic Jahn–Teller coupling of the orbitally degenerate ^{3}E state with (e) local modes of the $(MnO_4)^{3+}$ ion [23]. Such features are absent from the absorption spectra of Mn^{5+}-doped SVAP at 77 K.

5. Conclusions

The $3d^2$ ions have demonstrable potential as tunable laser-active ions in a variety of crystalline hosts in which the isoelectronic species V^{3+}, Cr^{4+} and Mn^{5+} occupy tetrahedral symmetry sites. In this study the V^{3+} and Mn^{5+} ions are fourfold coordinated with O^{2-} ions in the molecular ions $(VO_4)^{5-}$ and $(MnO_4)^{3-}$. In view of the odd-parity crystal field at these molecular ions in SVAP crystals the optical absorption transitions are very intense and cover much of the wavelength range 550–1000 nm. This would be ideal for diode-pumped laser action. Unfortunately, the $(VO_4)^{5-}$ ion decays non-radiatively such that no luminescence is observed. In contrast $(MnO_4)^{3-}$ in SVAP luminesces extremely efficiently at 300 K albeit via the sharp zero-phonon lines of the spin–orbit split $^1E \rightarrow {}^3A_2$ transition at $\sim$1.16 μm. This situation is rather similar to the R lines in ruby and as such would result in three-level laser operation. Nevertheless, the electric dipole nature of the absorption–luminescence transition and long lifetime (400 μs) at 300 K guarantees efficient laser action even at room temperature on the zero-phonon lines and their vibronic sidebands. Broadband tunability is not an option. There are other potential applications given the large damage threshold and thermal and chemical stability of SVAP: passive Q switching and sensitization for lanthanide ion lasers, especially Yb^{3+} and Er^{3+}.

Acknowledgments

This work was supported by a joint SERC:MoD rolling grant No GR/H/66143. One of us (MAS) is indebted to the SERC and the DRA (Malvern) for the award of a CASE Research Studentship.

Appendix. Analysis of selection rules in T_d, C_{3v} and C_s symmetries

The selection rules for the polarized absorption and photoluminescence spectra of the $3d^2$ ion in distorted tetrahedral sites may be determined using group theory. An x-ray diffraction analysis of the SVAP structure shows, from the lengths of the V^{5+}–O^{2-} bonds in table 1, that the $(VO_4)^{5-}$ co-ordination tetrahedron is distorted along the c axis. In consequence, the V^{5+} ion is off-centre, being further away from O(2) than from the other three O^{2-} ions. In apatite-like crystals the $(VO)_4$ tetrahedra are isolated from each other and are oriented differently. However, since they have a common mirror plane parallel to the a axis with the V–O(1) bond pointing along the [0001] axis, all of the tetrahedra are optically equivalent.

According to table 1 the symmetry of the local (VO_4) molecular ion is reduced from T_d to C_{3v} by an even-parity stretch along the c axis of the crystal. Other distortions of the apatite structure reduce the symmetry of the fourfold-coordinated site from C_{3v} to C_s [16]. From the character tables in table 2 of the T_d group there are two one-dimensional irreducible representations (A_1, A_2), one two-dimensional (E) and two threefold representations (T_1 and T_2). The C_{3v} group has only A_1, A_2 and E irreducible representations [9]. Reduction from C_{3v} to C_s symmetry, table 2, yields one-dimensional irreducible representations (A', A'') only.

The splitting pattern of the energy levels of the $3d^2$ ion is deduced by comparing the elements of the character tables of T_d, C_{3v} and C_s (table A1). For example, the splitting of the $^3T_2$ state in C_{3v} symmetry is determined by comparing the characters of the T_2 irreducible representations in T_d with those of the C_{3v} group. Since from table 2 $\chi^{T_2} = \chi^{A_1} + \chi^{E}$ the T_2 irreducible representation of the T_d group decomposes into A_1

Table A1. Character tables for the T_d, C_{3v} and C_s groups.

T_d	E	R	$4C_3$	$4C_3^2$	$3C_4^2$	$3S_4$	$3S_4^3$	$6\sigma_d$	
A_1	1	1	1	1	1	1	1	1	
A_2	1	1	1	1	1	−1	−1	−1	
E	2	2	−1	−1	2	0	0	0	
T_1	3	3	0	0	−1	1	1	−1	R_x, R_y, R_z
T_2	3	3	0	0	−1	−1	−1	1	x, y, z
C_{3v}	E	R	C_2^3	C_3^2	$3\sigma_v$	$3R\sigma_v$			
A_1	1	1	1	1	1	1			z
A_2	1	1	1	1	−1	−1			R_z
E	2	2	−1	−1	0	0			x, y, R_x, R_y
C_s	E	R	σ	σR					
A'	1	1	1	1					x, y, R_z
A''	1	1	−1	−1					z, R_x, R_y

and E irreducible representations in C_{3v} symmetry, each irreducible representation having a different energy. Hence, the $^3T_2$ level in T_d symmetry splits into $^3A_1$ and ^3E states in C_{3v} symmetry. Similarly, $^3T_1$ splits into $^3A_2$ and ^3E levels. In contrast, the $^3A_2$ ground state and ^1E excited states are not split in C_{3v} symmetry because the appropriate character elements are the same for both T_d and C_{3v} groups.

The additional orbital splittings caused by the further symmetry reduction $C_{3v} \varnothing C_s$ are determined by comparing the characters of the elements of the C_{3v} and C_s groups. From table 2 the singly degenerate levels A_1 and A_2 in C_{3v} symmetry are seen to transform as A' and A'' in C_s symmetry and the orbital doublets, E, in C_{3v} symmetry split into orbital singlets A' and A'' in C_s symmetry. The orbital splittings of the low-lying energy levels of $3d^2$ ions in tetrahedral sites are shown in figure 2 assuming T_d, C_{3v} and C_s symmetry.

The probability of a transition between the states Γ_1 and Γ_2 is proportional to the matrix element, $\langle \Gamma_1 | \boldsymbol{\mu} | \Gamma_2 \rangle$, where $\boldsymbol{\mu}$ is a dipole operator. Consequently, the selection rules for a transition $\Gamma_1 \times \Gamma_2$ are determined by comparing the function spaces in the character tables, table 2, which transform as the direct product $\Gamma_1 \times \Gamma_2$. The π- and σ-polarized electric dipole operators transform as z and $x\,y$ respectively, while the π- and σ-polarized magnetic dipole operators transform as R_x, R_y and R_z [9]. By inspection of table 2 the electric dipole (ED) operator is seen to transform as the irreducible representation, T_2, of the T_d group. Since $A_2 \times T_1 = T_2$, the only allowed electric dipole transition of the $3d^2$ ion is $^3A_2 \leftrightarrow {}^3T_1$; other electric dipole transitions are forbidden in tetrahedral symmetry. This transition is allowed in both π and σ polarizations.

From the character table for the C_{3v} group, the electric dipole operators transform as A_1 and E in π and σ polarizations, respectively. Furthermore, in π polarization the magnetic dipole operator transforms as the A_2 irreducible representation and the σ-polarized magnetic dipole operator transforms as the E irreducible representation. In consequence, the selection rules for all possible transitions in T_d symmetry, which are obtained from the direct products

$$\begin{aligned} &A_1 \times A_1 = A_1 \qquad A_2 \times A_1 = A_2 \qquad A_2 \times A_2 = A_1 \\ &A_1 \times E = E \qquad A_2 \times E = E \qquad E \times E = A_1 + A_2 + E \end{aligned} \tag{A1}$$

are as stated in table 3. These results show that the only allowed ED transitions from the $^3A_2$ ground state in C_{3v} symmetry are $^3A_2 \leftrightarrow {}^{2S+1}E$, $^{2S+1}A_2$ [9].

Returning to the case of C_s symmetry it is evident from the character table 2 that the ED(π) and MD(σ) operators transform as the A'' irreducible representation of the C_s group

whereas the ED(σ) and MD(π) operators transform as the A' irreducible representation. Applying

$$\begin{aligned} A' \times A' &= A' \qquad A' \times A' = A'' \\ A' \times A'' &= A'' \qquad A'' \times A'' = A' \end{aligned} \tag{A2}$$

gives the selection rules for C_s symmetry in table 3. Since the ground state of Mn^{5+} in C_s symmetry is $^3A''$, all optical transitions are partially allowed by the electric dipole mechanism, although the transition strengths depend also on the spin and configuration selection rules.

References

[1] Petricevic V, Gayen S K and Alfano R R 1989 *Appl. Opt.* **27** 4162
Petricevic V, Gayen S K and Alfano R R 1989 *Appl. Opt.* **28** 1610
[2] Casas-González J, Jacobsen S M, Hoffman K R and Yen W M 1991 *OSA Proc. on Advanced Solid State Lasers* ed G Dubé and L Chase **10** 64
[3] Petricevic V, Gayen S K and Alfano R R 1989 *Opt. Lett.* **14** 612
[4] Fratello V J, Brandle C D and Valentino A J 1987 *J. Cryst. Growth* **85** 229
[5] Caird J A, Krupke W F, Shinn M D, Smith L K and Wilder R E 1985 *CLEO Tech. Digest* **232**
[6] Angert N B, Borodin N I, Garmash V M, Zhitnyuk V A, Okhrimchuk A G, Siyuchenko O G and Schestakov A V 1988 *Sov. J. Quantum. Electron.* **18** 73
[7] Scott M A, Gallagher H G, Han T P J and Henderson B 1996 *J. Phys.: Condens. Matter* at press
[8] Sugano S, Tanabe Y and Kamimura H 1970 *Multiplets of Transition Metal Ions in Crystals* (New York: Academic)
[9] Henderson B and Imbusch G F 1989 *Optical Spectroscopy of Inorganic Crystals* (Oxford: Clarendon)
[10] Henderson B, Yamaga M and O'Donnell K P 1990 *Opt. Quantum Electron.* **22** S167
[11] Kingsley J D, Prener J S and Segall B 1965 *Phys. Rev.* A **137** 189
[12] Oetliker U, Herren M, Gudel H U, Kesper U, Albrecht C and Reinen D 1994 *J. Chem. Phys.* **100** 8696
[13] Merkle L D, Pinto A, Verdun H R and McIntosh B 1992 *Appl. Phys. Lett.* **61** 2386
Merkle L D, Guyot Y and Chai B H T 1995 *J. Appl. Phys.* **77** 474
[14] Scott M A 1995 *PhD Thesis* University of Strathclyde
[15] Corker D, Chai B H T, Nicholls J F H and Loutts G B 1995 *Acta Crystallogr.* C **51** 549
[16] Herren M, Gudel H U, Albrecht C and Reinen D 1991 *Chem. Phys. Lett.* **183** 98
[17] Morrison C A 1992 *Crystal Fields for Transition-Metal Ions in Laser Host Materials* (Berlin: Springer)
[18] Capobianco J A, Cormier G, Morrison C A and Moncorgé R 1992 *Opt. Mater.* **1** 209
[19] Capobianco J A, Cormier G, Bettinelli M, Moncorgé R and Manaa H 1992 *J. Lumin.* **54** 1
[20] Ballhausen C J 1962 *Introduction to Ligand Field Theory* (New York: McGraw-Hill)
[21] Rebane K K and Rebane L A 1975 *Optical Properties of Ions in Solids* ed B di Bartolo (New York: Plenum)
[22] Gonzales-Vilchez F and Griffiths W P 1972 *J. Chem. Soc. Dalton Trans.* 1416
[23] Day P, Borromei R and Oleari L 1981 *Chem. Phys. Lett.* **77** 214